water

MDPI

Article

Validation of GPM Precipitation Products by Comparison with Ground-Based Parsivel Disdrometers over Jianghuai Region

Zuhang Wu [1], Yun Zhang [1,*], Lifeng Zhang [1,*], Xiaolong Hao [2], Hengchi Lei [3] and Hepeng Zheng [1]

1 Department of Atmosphere Science and Engineering, College of Meteorology and Oceanography, National University of Defense Technology, Nanjing 211101, China; zuhangwu666@126.com (Z.W.); hepeng_z@163.com (H.Z.)
2 Beijing Tracking and Communication Technology Research Institute, Beijing 100000, China; haoxl@beidou.gov.cn
3 Institute of Atmospheric Physics, Chinese Academy of Sciences, Beijing 100000, China; leihc@mail.iap.ac.cn
* Correspondence: zhangyun.1207@yahoo.com (Y.Z.); zhanglif_qxxy@sina.cn (L.Z.); Tel.: +86-138-1410-2726 (Y.Z.); +86-135-1254-9105 (L.Z.)

Received: 5 May 2019; Accepted: 13 June 2019; Published: 16 June 2019

check for updates

Abstract: In this study, we evaluated the performance of rain-retrieval algorithms for the Version 6 Global Precipitation Measurement Dual-frequency Precipitation Radar (GPM DPR) products, against disdrometer observations and improved their retrieval algorithms by using a revised shape parameter μ derived from long-term Particle Size Velocity (Parsivel) disdrometer observations in Jianghuai region from 2014 to 2018. To obtain the optimized shape parameter, raindrop size distribution (DSD) characteristics of summer and winter seasons over Jianghuai region are analyzed, in terms of six rain rate classes and two rain categories (convective and stratiform). The results suggest that the GPM DPR may have better performance for winter rain than summer rain over Jianghuai region with biases of 40% (80%) in winter (summer). The retrieval errors of rain category-based μ (3–5%) were proved to be the smallest in comparison with rain rate-based μ (11–13%) or a constant μ (20–22%) in rain-retrieval algorithms, with a possible application to rainfall estimations over Jianghuai region. Empirical D_m–Z_e and N_w–D_m relationships were also derived preliminarily to improve the GPM rainfall estimates over Jianghuai region.

Keywords: satellite precipitation products; ground-based validation; precipitation; cloud physics

1. Introduction

Precipitation plays an important role in global climate systems and has significant spatial and temporal variability [1]. The accurate estimation of the global distribution of precipitation is crucial for the better performance of hydrological models [2]. The East Asian Summer Monsoon (EASM) is one of the most important rainfall systems that brings the major rainy season to East Asian countries [3–5]. Extreme rainfall events frequently occur over Jianghuai region (Figure 1) due to the impact from the East Asian Monsoon, and sometimes result in severe natural disasters like flash floods and mudslides [6–10]. Hence, the accurate prediction of precipitation in Jianghuai region is of great importance.

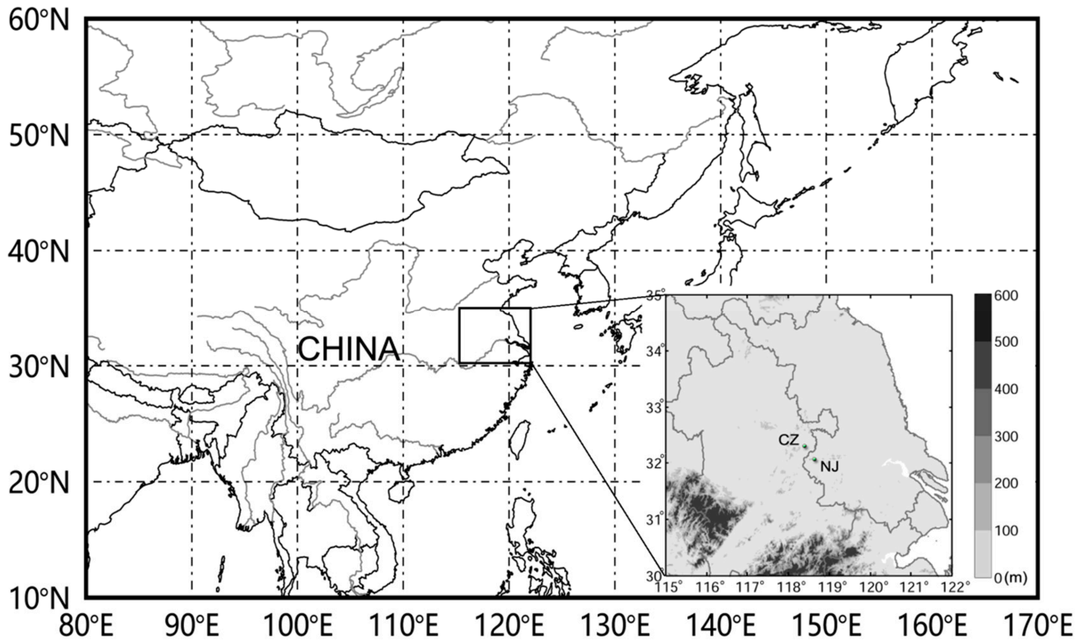

Figure 1. Locations of two observational sites (Nanjing (NJ) and Chuzhou (CZ)) over Jianghuai region. The superimposed rectangle represents Jianghuai region.

From ground-based gauges, disdrometers and radars to satellite-based sensors, the spatial and temporal variability of precipitation systems can be easily captured, particularly over rural areas where in situ measurements are scarce [11]. The Global Precipitation Measurement (GPM) mission, as a successor of the Tropical Rainfall Measuring Mission (TRMM), shows a significant advantage over gauge-based or radar-based estimates [12–14], which is expected to improve our knowledge of precipitation processes by providing greater dynamic range, more detailed information on microphysics, and better accuracy values in rainfall retrievals [15].

Raindrop size distribution (DSD) is the most fundamental microphysical property of precipitation. Extensive literature has revealed that the DSD characteristics vary with rain categories, geographical locations, storm to storm, and season to season [16–23]. Modeled DSD parameters are crucial for satellite-based rainfall estimation algorithms. For instance, three-parameter gamma distribution has been utilized in the GPM Dual-frequency Precipitation Radar (DPR) [24–26]. It was also reported by Tokay et al. [27] that the robust features of DSD parameters can be obtained from long-term observations of ground-based disdrometers and are useful in eliminating the assumptions of constant shape parameters in radar rainfall-retrieval and GPM DPR algorithms [25,26,28]. This motivated us to continue our research with this principle objective: the validation of GPM precipitation products using ground-based Parsivel disdrometers over Jianghuai region. It was found that DSD characteristics are highly affected by seasonal variations of precipitation in the Asian monsoon region [29]. Accordingly, seasonal DSD variability between summer and winter over Jianghuai region are studied, in terms of six rain rate classes and two rain categories (convective and stratiform). Optimized shape parameters under different seasons, rain rates and rain categories are obtained from the Parsivel observations over Jianghuai region. Furthermore, we revised the currently adopted shape parameter used in the GPM DPR with the results from our Parsivel observations and evaluated the performance of the new algorithm by comparison with the latest GPM precipitation products.

Following the introduction part, the data and methods are described in Section 2, the validation of GPM precipitation products are implemented in Section 3, and different GPM rainfall-retrieval methods are discussed in Section 4. Finally, Section 5 presents a summary and conclusions.

2. Data and Methods

2.1. Observational Sites and Datasets

Observations from in situ Parsivel disdrometers and GPM satellites are collected at Nanjing (NJ, 118.5° E, 32.0° N; 15 m ASL), Chuzhou (CZ, 118.3° E, 32.3° N; 18 m ASL). NJ and CZ stations are located in central Jianghuai region (Figure 1). Under the influence of the East Asian Monsoon, there are uneven distributions of rainfall in different seasons, causing significant microphysical variability between winter rain and summer rain [30]. In this paper, we separate the total rainfall samples into winter samples (December and January) and summer samples (June and July) for further research. The data used in this work are presented as follows:

2.1.1. In Situ Parsivel^2 Disdrometers

The 1-min DSD data selected for the analysis were measured by Parsivel^2 disdrometers from 2014 to 2018. The Parsivel^2 disdrometer used herein was a second-generation optical disdrometer manufactured by OTT Hydromet, Germany [31,32]. To minimize the measurement error, a data quality control procedure was implemented. Fallers with diameters over 8 mm or falling speeds outside ±60% of the empirical speed–diameter relationship for rain [33] were eliminated. In addition, 1-min samples with raindrop numbers less than 10 or rain rates less than 0.1 mm h^{-1} were excluded [27]. Following the definition of a rain event proposed by Tokay and Bashor [34], 48 rain events incorporating 52,056 1-min effective DSD samples were identified for the summer season, 53 rain events incorporating 16,831 samples were identified for the winter season. For simplicity, herein, we only listed the DSD data collected in 2014 (Table 1). Notably, the present study only focused on rainfall samples, to endorse that there were no snow samples or mix-phased particles in the winter season, a phase identification method (velocity and diameter relations) proposed by *Friedrich et al.* [35] was adopted herein (Figure 2).

Table 1. Precipitation events used for the present study in two seasons of 2014.

Seasons	Event No.	Date	Time (LST)	1-min Samples (min)	Accumulated Precipitation (mm)	Max Rain Rate (mm h^{-1})
Summer	1	15 Jun 2014	04:54–06:15	62	13.7	19.6
	2	15 Jun 2014	17:57–22:12	152	15.2	18.4
	3	16 Jun 2014	07:11–17:01	216	18.1	16.8
	4	25 Jun 2014	05:51–23:47	364	29.2	39.4
	5	26 Jun 2014	00:02–18:17	545	38.6	43.1
	6	1 Jul 2014	05:53–15:51	263	12.3	32.5
	7	1–2 Jul 2014	20:49–09:37	417	19.4	37.2
	8	4 Jul 2014	11:00–23:59	631	39.8	101.1
	9	5 Jul 2014	00:01–12:53	725	41.1	115.3
	10	12 Jul 2014	06:59–22:58	313	71.9	145.2
Winter	1	17 Dec 2014	11:10–13:36	146	3.5	3.9
	2	19 Dec 2014	12:24–20:02	192	5.9	2.9
	3	21 Dec 2014	10:24–21:42	99	0.2	0.6
	4	22–23 Dec 2014	12:10–01:47	130	0.1	0.4
	5	24 Dec 2014	14:25–20:43	67	0.1	0.2
	6	26 Dec 2014	06:41–12:52	120	2.5	6.9
	7	29 Dec 2014	09:52–10:58	66	1.1	2.8
	8	30 Dec 2014	15:23–23:02	328	12.8	6.8
	9	1 Jan 2015	04:02–09:28	189	4.9	3.1
	10	2–3 Jan 2015	13:05–06:44	205	9.7	4.3
	11	3 Jan 2015	08:21–16:37	156	2.4	1.6
	12	8 Jan 2015	15:34–16:57	83	3.5	2.8

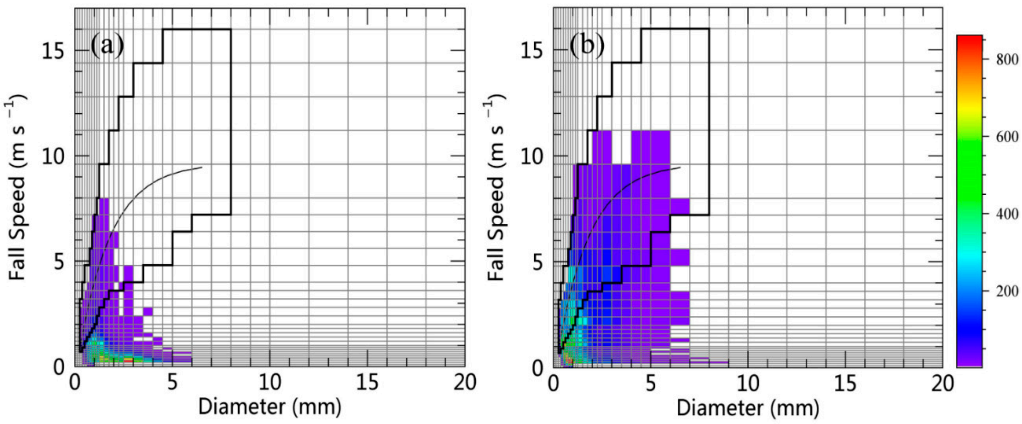

Figure 2. Identification and elimination of (**a**) snow sample case and (**b**) mix-phase sample case in total winter rainfall observations. The black curve represents the empirical fitting result of raindrops as reported by *Friedrich et al.* [35]. The black box represents rainfall area. The color mark represents particle number.

2.1.2. GPM DPR Level-2 Products

In this paper, three types of GPM DPR level-2 products, including the Ka-band high-sensitivity product (KaHS), Ku-band product (KuPR), and dual-frequency matched product (DPR_MS) are used to obtain the radar reflectivity and rain rate near the surface. The GPM DPR is comprised of a Ku-band precipitation radar (20 mm) and a Ka-band precipitation radar (8 mm). DPR scans are taken along and cross track of the spacecraft orbit (about 7 km s^{-1}) with a 5 × 5 km^2-footprint. It typically takes 1–2 min to cross the analysis domain (Figure 1). The matching between DPR and surface disdrometer observations depends both on the availability of the Parsivel composite and the presence of rainy events over the area. As a result, we have chosen 20 (25) effective observations from 40 (43) instantaneous cases in summer (winter) for the DPR–Parsivel comparisons. Table 2 simply shows the rain events observed by the GPM DPR during the summer season in June–July 2014 and the winter season in December–January 2015.

Table 2. Precipitation events observed by the Global Precipitation Measurement Dual-frequency Precipitation Radar (GPM DPR) when it overpasses Jianghuai region in two seasons of 2014.

Seasons	Pass No.	Date	Time (LST)	Rainfall Observations (√/×)	Max Rain Rate (mm h^{-1})
Summer	1	15 Jun 2014	02:56–04:29	√	10.2
	2	15 Jun 2014	12:11–13:44	×	0
	3	23 Jun 2014	00:41–02:13	×	0
	4	25 Jun 2014	23:39–01:11	√	24.3
	5	26 Jun 2014	08:54–10:27	√	32.1
	6	2 Jul 2014	06:50–08:23	√	19.5
	7	6 Jul 2014	20:21–21:54	×	0
	8	12 Jul 2014	04:24–05:56	√	62.4
Winter	1	9 Dec 2014	22:55–00:27	√	1.5
	2	10 Dec 2014	08:10–09:42	√	0.7
	3	18 Dec 2014	05:50–07:22	√	1.9
	4	20 Dec 2014	19:33–21:05	×	0
	5	21 Dec 2014	04:48–06:20	×	0
	6	23 Dec 2014	18:31–20:03	√	0.3
	7	26 Dec 2014	03:35–05:08	√	0.6
	8	8 Jan 2015	13:55–15:28	√	0.4
	9	10 Jan 2015	13:44–15:18	×	0
	10	13 Jan 2015	12:42–14:15	√	6.9
	11	27 Jan 2015	08:18–09:51	√	6.8

2.2. Raindrop Size Distribution

The raindrop size distribution is calculated from the Parsivel[2] disdrometer counts and the integral rainfall parameters, including the radar reflectivity factor Z (mm^6 m^{-3}), rain rate R (mm h^{-1}), rain water content W (g m^{-3}) and total concentration of raindrops N_t (mm^{-3}), are derived from measured DSDs as described in Wen et al. [36].

The three-parameter [N_0, μ and Λ] gamma function model is widely used to represent the measured raindrop spectra [37] and is expressed as

$$N(D) = N_0 D^{\mu} \exp(-\Lambda D) \tag{1}$$

where D (mm) is the raindrop diameter, N_0 is the intercept parameter, μ is the shape parameter, and Λ is the slope parameter. The truncated moment method has been well described in Wu et al. [22] to obtain the gamma model as well as other DSD parameters from Parsivel observations.

The standard deviation of the mass spectrum σ_M (mm), which can be used to measure the spectral width and shape of the DSD [38], is defined as

$$\sigma_M = \left[\frac{\sum\limits_{D_{\min}}^{D_{\max}} (D - D_m)^2 N(D) D^3 dD}{\sum\limits_{D_{\min}}^{D_{\max}} N(D) D^3 dD} \right]^{1/2} \tag{2}$$

where D_m (mm) is the mass-weighted mean diameter [39], given by

$$D_m = \frac{4 + \mu}{\Lambda} \tag{3}$$

The normalized gamma model has been proposed to solve the nonindependence problem of the parameters of gamma DSD model [39–42], which makes it possible to compare DSDs regardless of the time scale and rain rate and accurately examine the substantial variations associated with the physical rainfall regimes. We follow the normalized gamma DSD model as adopted in Wu et al. [22].

2.3. Calculated GPM DPR Variables

Based on the normalized gamma model, the effective radar reflectivity factor Z_e for each wavelength can be calculated as below:

$$Z_e = \frac{\lambda^4}{\pi^5 \left| k_w{}^2 \right|} \sum_{i=3}^{32} N(D_i) \sigma_b(D_i, \lambda) \Delta D_i \tag{4}$$

where λ is the radar wavelength and σ_b (D_i,λ) is the backscattering cross section of a raindrop with diameter D_i, which can be directly calculated based on Mie theory. $K_w{}^2$ is the dielectric factor, which is related to the complex refractive index of the region and is conventionally taken to be 0.93.

The difference between the dual-band reflectivity measurements is described by the dual-frequency ratio (DFR). The DFR (dB) is independent of the intercept parameter N_w and is defined as follows:

$$DFR = 10 \log_{10}\left(\frac{Z_{Ku}}{Z_{Ka}}\right) \tag{5}$$

where Z_{Ku} and Z_{Ka} are the effective radar reflectivity factors at Ku- and Ka-band frequencies, calculated via Equation (4).

2.4. GPM–Parsivel Comparison

For validation, GPM–Parsivel statistics [the normalized bias (NB) and the normalized standard error (NSE)] are computed with the following definitions:

$$NB = \frac{\sum(GPM - DSD)}{\sum DSD} \quad (6)$$

$$NSE = \frac{\sum|GPM - DSD|}{\sum DSD} \quad (7)$$

where *GPM* and *DSD* represent GPM DPR observation data and Parsivel measurement values, respectively (e.g., rain rate, reflectivity).

3. Validation of GPM Precipitation Products

The Ka–Ku DPR and the Microwave Imager (MI) onboard the GPM Core Observatory Satellite have been collecting data for several years, providing precipitation products over the globe, including oceans and remote areas where ground-based precipitation measurements are not available [43]. The validation work for the GPM constellation devotes significant effort and resources to improve the basic understanding required for physically based algorithms. Thus, we have compared concurrent DPR observations and Parsivel derivations in terms of mean rain rate and radar reflectivity near the surface.

In this work, we first selected the DPR_MS product to obtain the rain rate detected by DPR, due to the fact that the precipitation retrieval algorithm of DPR_MS is highly self-governed and performs better in retrieving both weak and intense rains than other algorithms [44–46]. Further, GPM DPR level-2 products, including KaHS and KuPR, were selected herein to obtain the observational single-band radar reflectivity factor for Ku and Ka band. The KaHS shows great advantages in observing weak precipitations, while KuPR performs well for intense precipitation observations [46].

Based on Parsivel^2 observations, we calculated the Ku-band (Ka-band) effective radar reflectivity factor Z_{Ku} (Z_{Ka}) for two seasons using Equation (4). Thereby, we can calculate the dual-frequency ratio (DFR) for the GPM–Parsivel comparison via Equation (5). The *DFR* provides valuable information that can be used to attain a better understanding of the microphysics associated with rain-retrieval algorithms. Thus, we analyzed and compared the relationship between the *DFR* and rain rate *R* from GPM and Parsivel observations. The comparison results are shown in Figure 3.

Figure 3 shows an example of the scatterplots near the surface from both DPR observations (Figure 3, left) and DSD derivations (Figure 3, right) for two seasons. At higher rain rates (deep convective rain), the *DFR* may reach an equilibrium state, where Z_{Ku} and Z_{Ka} are in linear correlation. The values of the *DFR* from observation and derivation remain nearly constant at approximately 0.3 and 0.5 (dB) for winter, 0.1 and 0.5 (dB) for summer, respectively. We computed the GPM–Parsivel normalized bias (NB) via Equation (6). The comparison results (NB = 0.4 for winter, NB = 0.8 for summer) suggest that the GPM underestimate the *DFR* more in the summer season than in the winter season, which indicates that the GPM might have better performance for winter rain than summer rain over Jianghuai region.

Particularly, the GPM DPR observations show a distinct lower frequency ratio of strong convective echoes compared with those from Parsivel (Figure 3). Except for the attenuation caused by multiple scattering, the possible reason for such a discrepancy could be the impact of nonuniform beam filling on DPR estimates of convective echoes, which affects not only errors in the estimate of path attenuation but also the retrieval of microphysical parameters regarding the properties (phase state, shape, nonuniform distributions, etc.) of precipitation particles [47]. In addition, due to the broader spectral width of the precipitation during summer than that of winter, the discrepancy would be worse in the summer season.

To explain the unique characteristics above, the σ_M–D_m variations of the observed DSD samples in two seasons are analyzed via Equations (2) and (3) and are shown in Figure 4. These variations are represented in terms of the frequency of occurrence, as joint PDF where the colors represent the number of cases with the corresponding σ_M–D_m pairs. In two seasons, a similar variation is found that σ_M generally increases with D_m. The variation for each part precipitation samples was fitted to a power law, and the fitted curve is superimposed on a corresponding plot in Figure 4. The fitted power law equation for winter is given by:

$$\sigma_M = 0.295 {D_m}^{1.50} \tag{8}$$

for summer, it is given by:

$$\sigma_M = 0.275 {D_m}^{1.36} \tag{9}$$

Comparing the two seasons, though winter precipitation has a larger exponent for σ_M–D_m relations, the mean values of σ_M and D_m are smaller in winter rain than summer rain (σ_M = 0.38, D_m = 1.31 for winter and σ_M = 0.40, D_m = 1.44 for summer), resulting in a broader spectral width with more large droplets in summer. In addition, this further implies the microphysics variability between different seasons.

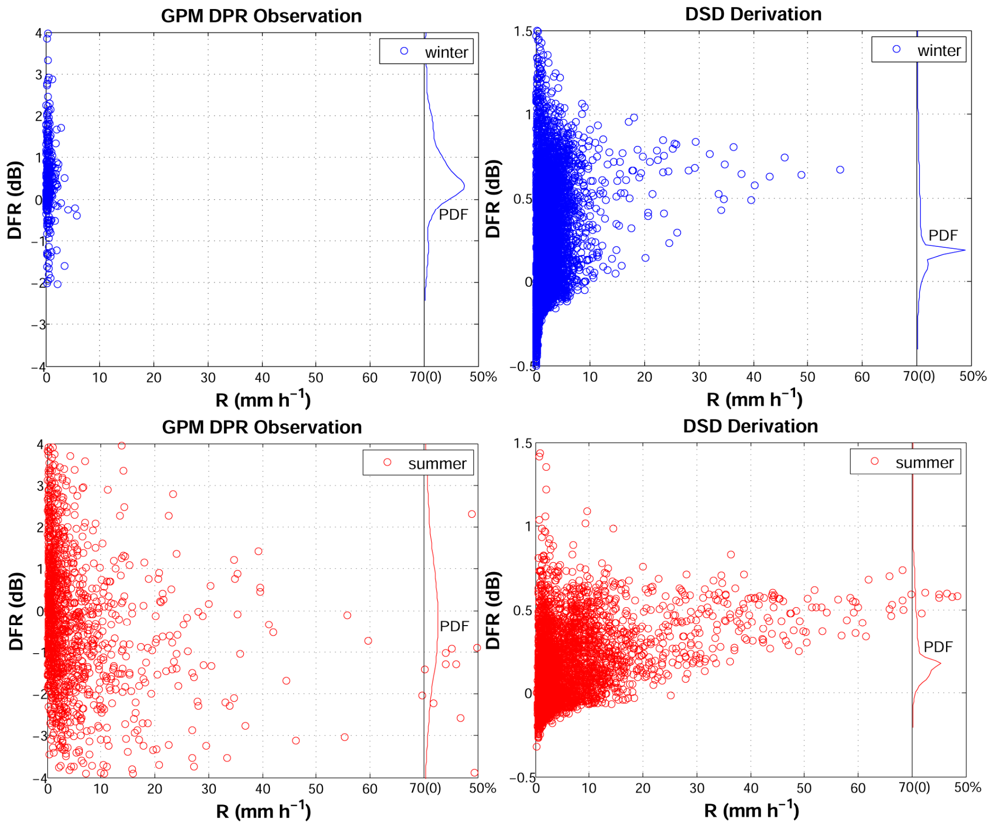

Figure 3. Scatterplots of the dual-frequency ratio (DFR) versus rain rate from DPR observations and raindrop size distribution (DSD) derivations on the same scale during winter (blue circles) and summer (red circles) over Jianghuai region. The left two panels represent results from GPM observations, and the right two panels represent results from DSD derivations. The probability density functions (PDF) of the DFR are also given in each panel.

To compare our data with those of other climatic regimes reported in Bringi et al. [48], Figure 5 shows the values of $log_{10}(N_w)$ versus D_m for the convective and stratiform rain types over Jianghuai region. The two outlined boxes on the scatterplot correspond to the maritime-like and continental-like convective clusters as defined by Bringi et al. [48]. Note that the stratiform rain samples of both seasons are very close to the stratiform line reported by Bringi et al. [48]. The convective precipitation in summer can be identified as both maritime-like and continental-like, which could be related to the abundant moisture transported from tropical ocean during summer, while that of winter is close to continental-like convective precipitation. In addition, this could be due to the typical dry and cold weather during winter monsoon season over Jianghuai region.

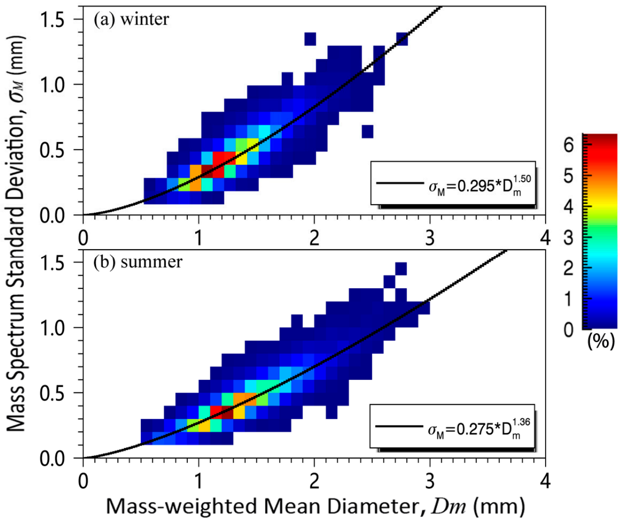

Figure 4. σ_M–D_m two-dimensional PDF distributions and fitting results based on Parsivel disdrometer observations in two seasons. The resolution of PDF is 0.1 mm × 0.1 mm and the color mark value represents the frequency of occurrence (%) of σ_M versus D_m.

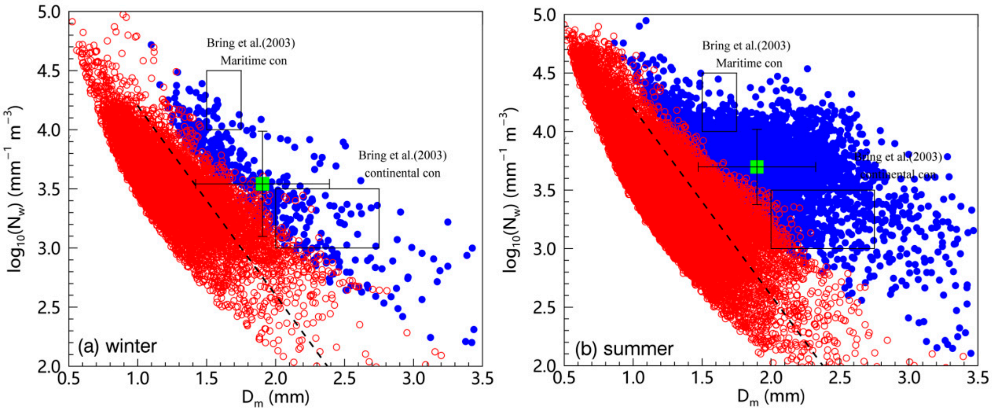

Figure 5. Distribution of $log_{10}(N_w)$ and D_m observed from the Parsivel disdrometer for convective (blue filled circles) and stratiform precipitation (red hollow circles) during (**a**) winter and (**b**) summer over Jianghuai region (along with ± standard deviation). The green symbol represents the average value of convective rain. The two outlined rectangles correspond to the maritime and continental convective clusters reported by Bringi et al. [48]. The black dashed line indicates the fitting result of stratiform rain [48].

4. Improvement of GPM Retrieval Algorithms

Though spaceborne radars show great advantages, the rainfall retrieval algorithm of the GPM DPR is not yet mature. A physically based algorithm requires greater insight into the properties and behavior of both ice microphysics and land surface processes. Surface disdrometers could be employed to improve the retrieval algorithms locally by providing detailed particle microphysical information (sizes, shapes, types, numbers, etc.). In this study, we employ Parsivel measurements to develop constraints that are optimized for DPR retrieval algorithms with possible application to rainfall estimation over Jianghuai region.

The *DFR* is usually used for the retrieval of D_m. Nevertheless, when the *DFR* is negative, D_m cannot be uniquely retrieved because of the well-known "dual value" problem as indicated in *Meagher and Haddad* [49], which is an obstacle for dual-frequency radar DSD retrievals. For our data, the dual-valued phenomenon also existed (Figure 3). To avoid such a dual-value problem, only the effective radar reflectivity was used in this work to obtain the empirical relationship of D_m.

Based on disdrometer observations during two seasons, scatter plots and fitting results of D_m–Z_{Ku}, D_m–Z_{Ka} and $log_{10}(N_w)$–D_m were obtained as shown in Figure 6. D_m increase tends to be highly correlated with increasing Z_{Ku} or Z_{Ka}. There is an inverse relationship between $log_{10}(N_w)$ and D_m. Following a least squares method, we derived the second-degree polynomial relationships of D_m–Z_{Ku}, D_m–Z_{Ka} and $log_{10}(N_w)$–D_m as presented in Table 3. Using the three relations, the parameters N_w and D_m can be derived first. Then combined with the normalized gamma model described in Section 2.2, the DSD can be preliminarily reconstructed from the derived N_w and D_m given a local μ value. Thereby, the rain rate can be estimated eventually with the derived DSD. It was reported by Liao et al. [25] that a fixed-μ value (μ = 3) generally yields the smallest error. However, a single constant μ value may not exist. To acquire an optimized shape parameter, statistical results of gamma model parameters under different seasons, rain rates and rain categories are obtained from the Parsivel observations over Jianghuai region. The results are evaluated by comparison with Parsivel observations.

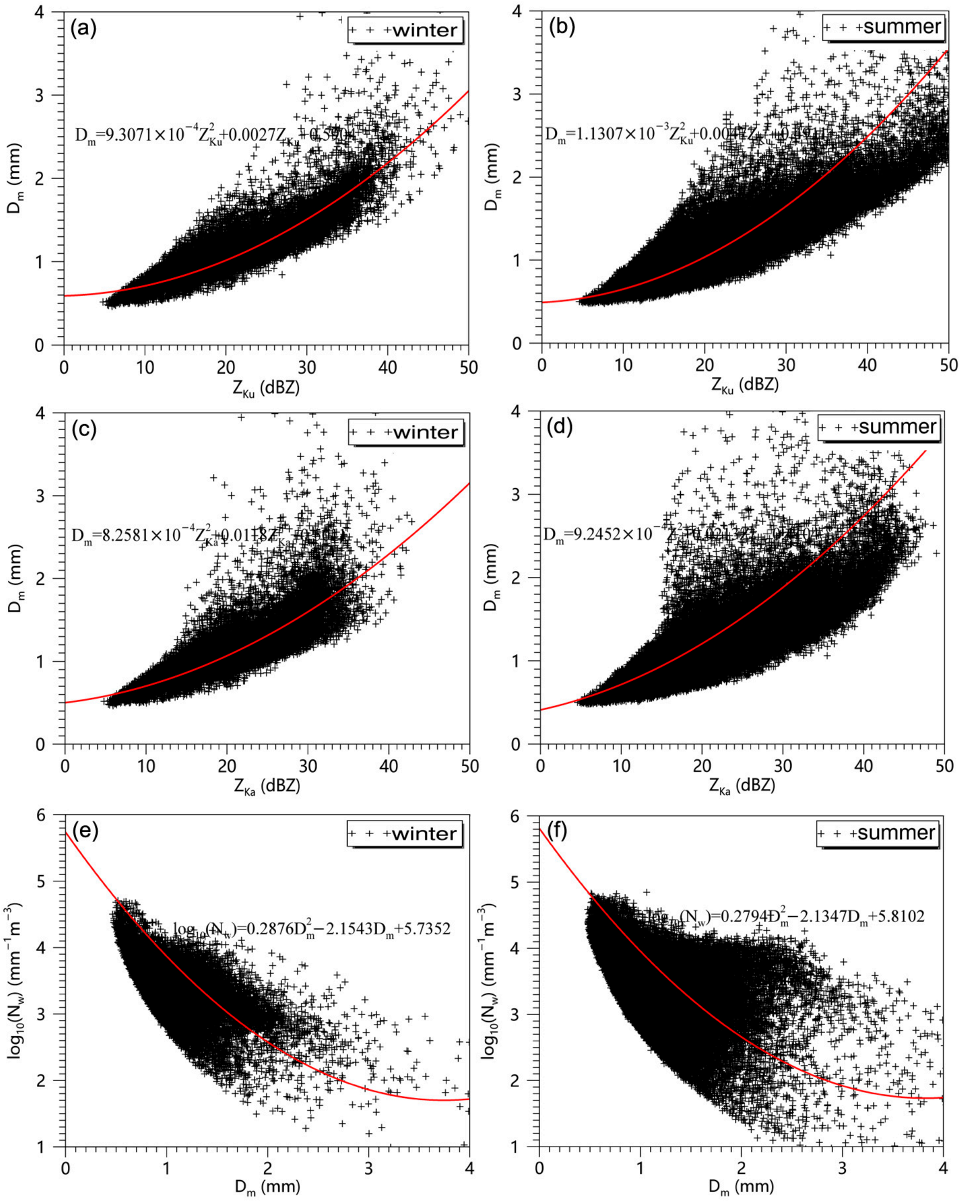

Figure 6. Scatterplots of D_m (mm) and Z_{Ku} (dBZ); D_m (mm) and Z_{Ka} (dBZ); $log_{10}(N_w)$ (mm^{-1}m^{-3}) and D_m (mm) derived from the Parsivel disdrometer data for two seasons. The left ones stand for winter and the right ones for summer. The overlaid red lines represent the fitted curves.

Table 3. Second-degree polynomial relationships of D_m–Z_{Ku}, D_m–Z_{Ka} and $log_{10}(N_w)$–D_m derived in two seasons.

Relation	Data	a	b	c
$D_m = \mathrm{a}{Z_{Ku}}^2 + \mathrm{b}Z_{Ku} + \mathrm{c}$	Winter Summer	0.00093071 0.00113070	0.0027 0.0047	0.5904 0.4911
$D_m = \mathrm{a}{Z_{Ka}}^2 + \mathrm{b}Z_{Ka} + \mathrm{c}$	Winter Summer	0.00082581 0.00092452	0.0118 0.0213	0.5011 0.4104
$log_{10}(N_w) = \mathrm{a}{D_m}^2 + \mathrm{b}D_m + \mathrm{c}$	Winter Summer	0.2876 0.2794	–2.1543 –2.1347	5.7352 5.8102

4.1. Under Different Rain Rates

To discern the precipitation differences between two seasons, the DSD samples are stratified into six rain rate classes: R ≤ 2, 2 < R ≤ 5 [1], 5 < R ≤ 10, 10 <R ≤ 20, 20 < R ≤ 40, and R > 40 mm h^{-1} and large (small) drops are assumed to be D > 4 (D < 1) mm. The average raindrop spectra of two seasons in six rain rates are shown in Figure 7, which suggests that the particle number concentration and spectral width both increase with an increase in rain rate. Comparing the two seasons, the concentration of large drops is larger in winter season than summer season at the same rain rate class, which could be due to a stronger collision–coalescence process within small drops as well as the easier evaporation of small drops in drier winter conditions. The concentration of small drops is larger in the summer season than in the winter season, with an increase in rain rate that could be due to the stronger collision–breakup process within large drops.

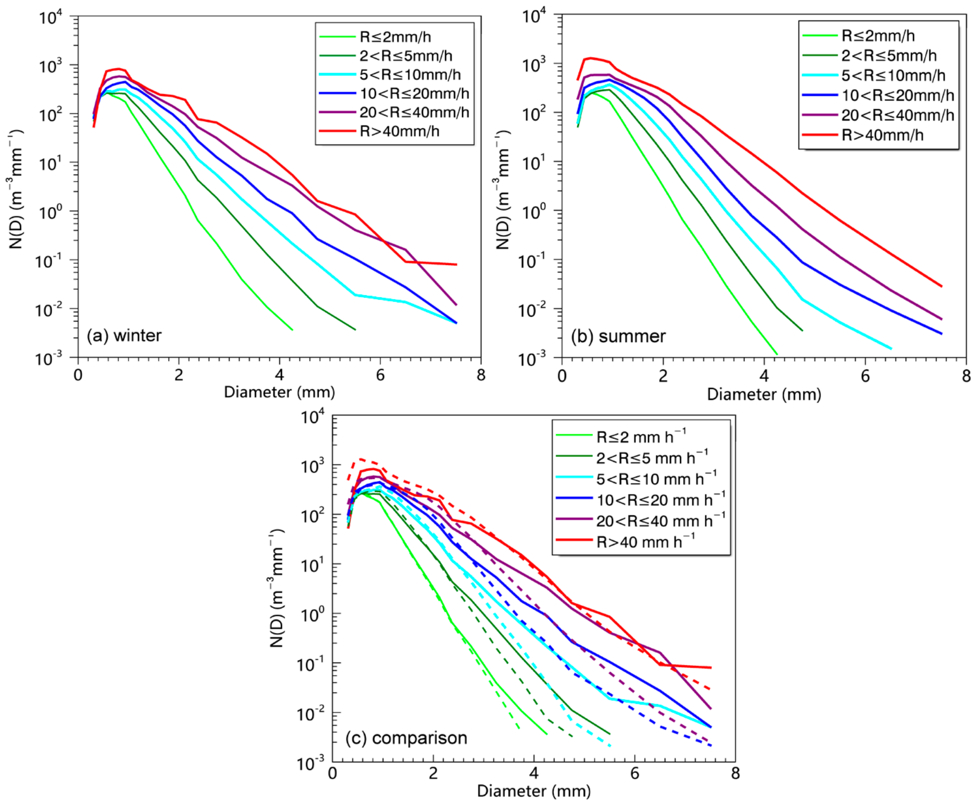

Figure 7. The average DSDs from the Parsivel disdrometer data at six indicated rain rate classes in two seasons, as well as their comparison result, where dotted lines represent summer rainfall and solid lines represent winter rainfall.

Table 4 provides the mean values of gamma model parameters under different rain rates. It is notable that N_0 and λ both increase with an increase in rain rate, while μ values increase to a maximum value first, then decrease to a minimum value. Comparing the two seasons, the three parameters of summer rain are slightly larger than winter rain at the same rain rate class. Such a difference could be attributed to the different rain categories in two seasons. The convective rain of the summer season was fed with moisture transported by the southwesterly monsoon. The winter rain is impacted by the northeasterly monsoon, causing large-scale frontal rainfall.

Table 4. Mean values of gamma distribution parameters in terms of six rain rate classes.

Season	Rain Rate Class	$\log_{10}N_0$	μ	Λ
Winter	$R \leq 2$	4.82	3.09	5.85
	$2 < R \leq 5$	4.71	2.88	5.04
	$5 < R \leq 10$	4.45	3.14	4.28
	$10 < R \leq 20$	4.27	3.52	4.14
	$20 < R \leq 40$	4.11	1.87	2.88
	$R > 40$	3.91	1.22	2.41
Summer	$R \leq 2$	4.86	3.20	6.01
	$2 < R \leq 5$	4.73	3.41	5.23
	$5 < R \leq 10$	4.65	3.79	5.01
	$10 < R \leq 20$	4.42	3.61	4.55
	$20 < R \leq 40$	4.27	2.85	3.54
	$R > 40$	3.98	1.34	2.39

Based on the μ value obtained at different rain rates (Table 4), we derived the DSD using D_m–Z_{Ku}, D_m–Z_{Ka} and $log_{10}(N_w)$–D_m relationships and calculated the rain rate. The NB and NSE statistics are also computed via Equations (6) and (7) for evaluation (Table 5). Compared with a constant μ in Liao et al. [25], the rain rate-based μ performs better in Jianghuai region with a NB of −11.3% and a NSE of 33.2% for winter, and a NB of −13.1% and a NSE of 36.3% for summer.

Table 5. Statistical results of the GPM–Parsivel comparison for rain rate given as a constant μ, μ under different rain rates, as well as μ under different rain categories. NB and NSE (%) represent normalized bias and normalized standard error, respectively.

	Season	NB (%)	NSE (%)
$\mu = 3$	Winter	−20.7	58.3
	Summer	−22.1	60.5
μ (rain rate-based)	Winter	−11.3	33.2
	Summer	−13.1	36.3
μ (rain category-based)	Winter	−3.5	17.9
	Summer	−5.3	18.8

4.2. Under Different Rain Categories

To study the DSD characteristics of different rain types, the 1-min samples were further categorized into two types (convective and stratiform). Several rainfall classification methods have been well developed based on disdrometer observations [16,39,48]. However, the result of Tokay and Short [16] was obtained from tropical rainfall clusters, which is inappropriate for our study due to different regional characters. The categorization method of Testud et al. [39] was based on the variability of rain rate (R) with time. In addition, the categorization method of Bringi et al. [48] was based on the standard deviation value (σ_R) of the rain rate. In this work, two categorization schemes are combined together to separate total samples into convective and stratiform clusters. Specifically, for ten consecutive 1-min samples, if the R values of ten adjacent values are all less than 10 mm h^{-1} and the standard deviation

σ_R is less than 1.5 mm h^{-1}, then the rain is defined as stratiform, otherwise it is classified as convective clusters. Consequently, winter and summer consist of 94.7% (5.3%), 80% (20%) stratiform (convective) rainfall samples, respectively. The results indicate a dominant stratiform rain type in winter.

The average DSDs of the two rain types are described in Figure 8. Comparing the convective rain in the two seasons, summer rain contains more sufficient droplets than winter rain, which could be due to the stronger convective activity during summer. Further, the gamma model statistics are listed in Table 6. Comparing the two seasons, the three parameters [N_0, μ and Λ] of the gamma model all exhibit larger values in summer than winter—both for convective rain and stratiform rain. Comparing the two rain types, the stratiform rain shows larger values of [N_0, μ and Λ] than convective rain.

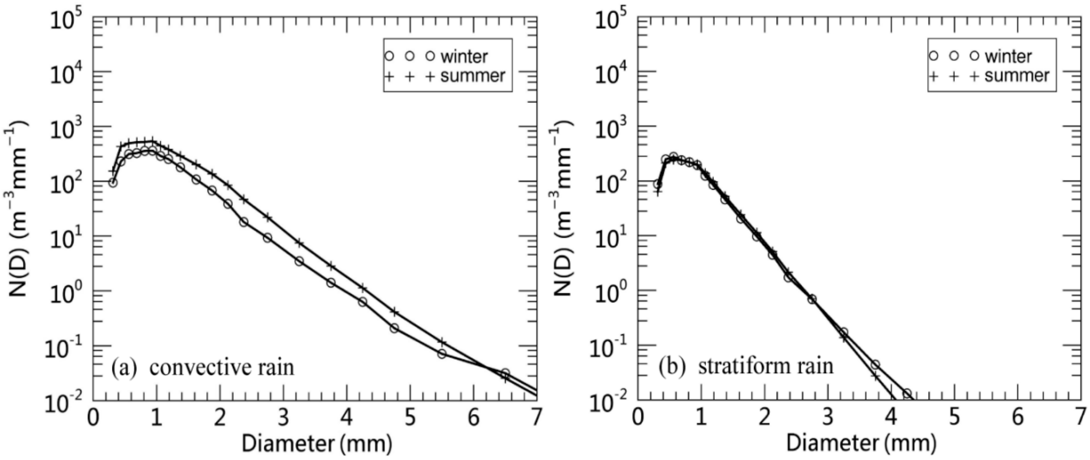

Figure 8. The average DSDs of two indicated rain types: (**a**) convective rain, (**b**) stratiform rain.

Table 6. Statistical results of gamma model parameters in terms of two rain types. SD and SK represent standard deviation and skewness, respectively.

Rain Type	Season	$\log_{10}N_0$			μ			Λ		
		Mean	**SD**	**SK**	**Mean**	**SD**	**SK**	**Mean**	**SD**	**SK**
Convective	Winter	4.26	1.39	0.79	3.81	3.31	0.89	4.37	2.68	1.07
	Summer	4.70	1.14	0.73	4.69	2.92	0.69	4.89	2.42	0.94
Stratiform	Winter	5.12	1.50	0.38	4.66	2.93	0.56	6.94	3.22	0.49
	Summer	5.41	1.45	0.34	5.92	2.87	0.38	7.60	3.07	0.44

Based on the μ value obtained at different rain categories (Table 6), we derived the DSD using D_m–Z_{Ku}, D_m–Z_{Ka} and $log_{10}(N_w)$–D_m relationships and calculated the rain rate. The NB and NSE statistics are also computed via Equations (6) and (7) for evaluation (Table 5). Compared with a constant μ or a rain rate-based μ, the rain category-based μ performs best in Jianghuai region with a NB of −3.5% and a NSE of 17.9% for winter, and a NB of −5.3% and a NSE of 18.8% for summer.

4.3. Possible Application of the μ–Λ Relationship

The μ–Λ empirical relationship has been widely demonstrated to better describe the DSD variability in natural rain ([50,51]. Studies have also shown that radar rainfall estimations improve after adjusting the μ–Λ relationship to ground observations [52]. In recent years, it was found that the μ–Λ relationship varies within different precipitation types, different climate regimes and different terrains [50–54]. Zhang et al. [50] obtained the μ–Λ relationship in Florida using DSD data collected in summer. Chen et al. [51] obtained the μ–Λ relationship in Nanjing during Meiyu. It needs to be customized in order to obtain the unique μ–Λ relationships for precipitation during different seasons.

Following the data processing method of Zhang et al. [50], the samples with rain rate $R > 5$ mm h^{-1} and number concentration $N > 1000$ were fitted by the truncated moment method to obtain μ

and Λ values in two seasons. A second-degree polynomial μ–Λ relationship was further derived. The relationship for winter is:

$$\Lambda = 0.053\mu^2 + 0.437\mu + 1.540 \tag{10}$$

The relationship for summer is:

$$\Lambda = 0.017\mu^2 + 0.724\mu + 1.958 \tag{11}$$

and the results are shown in Figure 9. Given the same Λ, we notice the parameter μ of winter is less than that of summer. Such differences could be due to the relatively higher concentration of small drops in summer. For a gamma model, the μ–Λ relationship can be also expressed as $\Lambda D_m = 4 + \mu$ [39]. Thus, given the D_m and μ values, the corresponding Λ value can be estimated. As shown in Figure 8, compared to the fit of convective rain from *Chen et al.* [51], our fits appear in the lower D_m region, which suggests that the DSDs in Meiyu precipitation have higher D_m values than those observed in Jianghuai region.

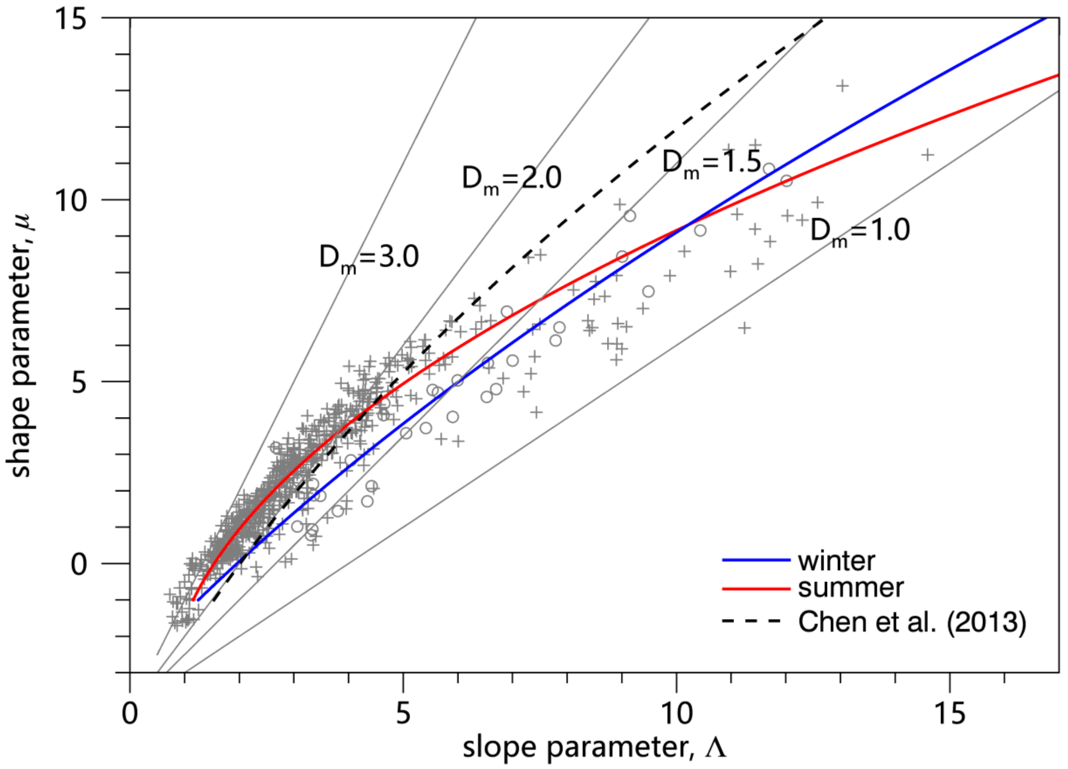

Figure 9. μ–Λ relationship scatterplots and fitting curves based on Parsivel disdrometer observations in two seasons. The gray circles represent winter precipitation samples and the gray crosses represent summer precipitation samples. The dashed line represents the empirical μ–Λ relationship of convective rain during Meiyu from *Chen et al.* [51]. The gray lines correspond to the relationship $\Lambda D_m = 4 + \mu$ [39] given the value of D_m = 1.0, 1.5, 2.0, and 3.0 mm.

To diminish the retrieval errors from assuming a constant shape parameter, a μ–Λ relationship can be imposed [55]. Thus, a native μ–Λ relationship could possibly be applied to improve GPM DPR rainfall estimates in a specific area (herein Jianghuai region). By using the μ–Λ relationship obtained in Jianghuai, as well as Equation (3), μ and Λ can be solved with the D_m value calculated from D_m–Z_e relationships presented in Table 3, given a reflectivity factor. Therefore, the rain rate can be eventually estimated with the derived normalized gamma model as described in Section 2.2. The performance of DSD retrieval using the above three equations should be assessed. However, the retrieval is mostly theoretical and needs more research in future work.

5. Summary and Conclusions

In this work, we studied seasonal DSD variability between summer and winter over Jianghuai region using measurements taken from Parsivel disdrometers, as well as GPM observations. The validation and improvement of GPM precipitation products are implemented based on the DSD properties. The major conclusions can be drawn as below:

1. GPM underestimates the *DFR* more in summer than winter, which indicates that GPM might have better performance in the winter than summer season over Jianghuai region with biases of 40% (80%) in winter (summer). Such a discrepancy could be due to the broader spectral width of the precipitation during summer than that of winter in this specific area.
2. The shape parameters μ under different rain rates as well as rain categories are obtained from 5-year Parsivel observations over Jianghuai region. The retrieval errors of rain category-based μ (3–5%) are proved to be smaller than that of rain rate-based μ (11–13%) or a constant μ (20–22%) in rain-retrieval algorithms, with a possible application to rainfall estimations over Jianghuai region.
3. The effective radar reflectivity factor Z_e is calculated using Parsivel disdrometer data. Empirical D_m–Z_e and N_w–D_m relationships are further derived to improve the GPM rainfall estimates over Jianghuai region.

Author Contributions: Conceptualization, Y.Z. and Z.W.; methodology, Z.W.; software, L.Z.; validation, Z.W., Y.Z. and L.Z.; formal analysis, Z.W.; investigation, X.H.; resources, Y.Z.; data curation, H.L.; writing—original draft preparation, Z.W.; writing—review and editing, H.Z.; visualization, X.H.; supervision, Y.Z.; project administration, L.Z.; funding acquisition, L.Z.

Funding: This research was financially supported by the Beijige Open Research Fund for Nanjing Joint Center of Atmospheric Research (NJCAR2018ZD03). The article processing charge (APC) was funded by NJCAR2018ZD03.

Conflicts of Interest: The authors declare no conflict of interest.

References

1. Ning, S.; Wang, J.; Jin, J.; Ishidaira, H. Assessment of the Latest GPM-Era High-Resolution Satellite Precipitation Products by Comparison with Observation Gauge Data over the Chinese Mainland. *Water* **2016**, *8*, 481. [CrossRef]
2. Ma, Z.; Tan, X.; Yang, Y.; Chen, X.; Kan, G.; Ji, X.; Lu, H.; Long, J.; Cui, Y.; Hong, Y. The First Comparisons of IMERG and the Downscaled Results Based on IMERG in Hydrological Utility over the Ganjiang River Basin. *Water* **2018**, *10*, 1392. [CrossRef]
3. Tao, S.; Chen, L. A review of recent research on the East Asian summer monsoon in China. In *Monsoon Meteorology*; Chang, C.-P., Krishnamurti, T.N., Eds.; Oxford University Press: London, UK, 1987; pp. 60–92.
4. Ding, Y.H.; Chan, J.C.L. The East Asian summer monsoon: an overview. *Meteor. Atmos. Phys.* **2005**, *89*, 117–142.
5. Ha, K.J.; Heo, K.Y.; Lee, S.S.; Yun, K.S.; Jhun, J.G. Variability in the East Asian Monsoon: A review. *Meteorol. App.* **2012**, *19*, 200–215. [CrossRef]
6. Ninomiya, K.; Shibagaki, Y. Cloud system families in the Meiyu-Baiu front observed during 1–10 July 1991. *J. Meteor. Soc. Japan* **2003**, *81*, 193–209. [CrossRef]
7. Kato, T.; Aranami, K. Formation factors of 2004 Niigata-Fukushima and Fukui heavy rainfalls and problems in the predictions using a cloud-resolving model. *SOLA* **2005**, *1*, 1–4. [CrossRef]
8. Kato, T. Structure of the band-shaped precipitation system inducing the heavy rainfall observed over northern Kyushu, Japan on 29 June 1999. *J. Meteor. Soc. Japan* **2006**, *84*, 129–153. [CrossRef]
9. Li, Q.; Wei, F.; Li, D. Interdecadal variation of East Asian summer monsoon and drought/flood distribution over eastern China in the last 159 years. *J. Geogr. Sci.* **2011**, *21*, 579–593. [CrossRef]
10. Shan, X.; Jiang, N.; Qian, W. Regional heavy rain locations associated with anomalous convergence lines in eastern China. *Nat. Hazards* **2015**, *77*, 1731–1750. [CrossRef]
11. Tong, K.; Zhao, Y.; Wei, Y.; Hu, B.; Lu, Y. Evaluation and Hydrological Validation of GPM Precipitation Products over the Nanliu River Basin, Beibu Gulf. *Water* **2018**, *10*, 1777. [CrossRef]

12. Hou, A.Y.; Kakar, R.K.; Neeck, S.; Azarbarzin, A.A.; Kummerow, C.D.; Kojima, M.; Oki, R.; Nakamura, K.; Iguchi, T. The Global Precipitation Measurement Mission. *Bull. Am. Meteorol. Soc.* **2014**, *95*, 701–722. [CrossRef]
13. Huffman, G.J.; Bolvin, D.T.; Nelkin, E.J. Integrated Multi-Satellite Retrievals for GPM (IMERG) Technical Documentation. 2015. Available online: https://pmm.nasa.gov/sites/default/fifiles/document_fifiles/IMERG_doc.pdf (accessed on 22 March 2019).
14. Gilewski, P.; Nawalany, M. Inter-Comparison of Rain-Gauge, Radar, and Satellite (IMERG GPM) Precipitation Estimates Performance for Rainfall-Runoff Modeling in a Mountainous Catchment in Poland. *Water* **2018**, *10*, 1665. [CrossRef]
15. Le, M.; Chandrasekar, V. Hydrometeor Profile Characterization Method for Dual-Frequency Precipitation Radar Onboard the GPM. *IEEE Trans. Geosci. Remote Sens.* **2013**, *51*, 3648–3658. [CrossRef]
16. Tokay, A.; Short, D.A. Evidence from tropical raindrop spectra of the origin of rain from stratiform versus convective clouds. *J. Appl. Meteorol.* **1996**, *35*, 355–371. [CrossRef]
17. Kumar, S.B.; Reddy, K.K. Raindrop size distribution characteristics of cyclonic and north east monsoon thunderstorm precipitating clouds observed over Kadapa (14.47°N, 78.82°E), tropical semi-arid region of India. *Mausam* **2013**, *64*, 35–48.
18. Kumari, N.P.A.; Kumar, S.B.; Jayalakshmi, J.; Reddy, K.K. Raindrop size distribution variations in JAL and NILAM cyclones induced precipitation observed over Kadapa (14.47°N, 78.82°E), a tropical semi-arid region of India. *Indian J. Radio Space Phys.* **2014**, *43*, 57–66.
19. Seela, B.K.; Janapati, J.; Lin, P.-L.; Reddy, K.K.; Shirooka, R.; Wang, P.K. A comparison study of summer season raindrop size distribution between Palau and Taiwan, two islands in western Pacifific. *J. Geophys. Res. Atmos.* **2017**, *122*, 11787–11805. [CrossRef]
20. Dolan, B.; Fuchs, B.; Rutledge, S.A.; Barnes, E.A.; Thompson, E.J. Primary modes of global drop-size distributions. *J. Atmos. Sci.* **2018**, *75*, 1453–1476. [CrossRef]
21. Wang, D.; Giangrande, S.E.; Bartholomew, M.J.; Hardin, J.; Feng, Z.; Thalman, R.; Machado, L.A.T. The Green Ocean: Precipitation insights from the GoAmazon2014/5 experiment. *Atmos. Chem. Phys.* **2018**, *18*, 9121–9145. [CrossRef]
22. Wu, Z.; Zhang, Y.; Zhang, L.; Lei, H.; Xie, Y.; Wen, L.; Yang, J. Characteristics of summer season raindrop size distribution in three typical regions of western Pacific. *J. Geophys. Res. Atmos.* **2019**, *124*, 4054–4073. [CrossRef]
23. Giangrande, S.E.; Wang, D.; Bartholomew, M.J.; Jensen, M.P.; Mechem, D.B.; Hardin, J.C.; Wood, R. Midlatitude oceanic cloud and precipitation properties as sampled by the ARM Eastern North Atlantic Observatory. *J. Geophys. Res. Atmos.* **2019**, *124*, 4741–4760. [CrossRef]
24. Hou, A.Y.; Skofronick-Jackson, G.; Kummerow, C.D.; Shepherd, J.M. Global precipitation measurement. In *Precipitation: Advances in Measurement, Estimation and Prediction*; Michaelides, S., Ed.; Springer: New York, NY, USA, 2008; pp. 131–169.
25. Liao, L.; Meneghini, R.; Tokay, A. Uncertainties of GPM DPR rain estimates caused by DSD parameterizations. *J. Appl. Meteor. Climatol.* **2014**, *53*, 2524–2537. [CrossRef]
26. Nakamura, K.; Iguchi, T. Dual-wavelength radar algorithm. In *Measuring Precipitation from Space*; Levizanni, V., Bauer, P., Turk, F.J., Eds.; Springer: New York, NY, USA, 2007; pp. 225–234.
27. Tokay, A.; Petersen, W.A.; Gatlin, P.; Wingo, M. Comparison of raindrop size distribution measurements by collocated disdrometers. *J. Atmos. Oceanic. Technol.* **2013**, *30*, 1672–1690. [CrossRef]
28. Brandes, E.A.; Zhang, G.; Vivekanandan, J. Experiments in rainfall estimation with a polarimetric radar in a subtropical environment. *J. App. Meteorol.* **2002**, *41*, 674–685. [CrossRef]
29. Kozu, T.; Akramin, Z.; Shimomai, T. Seasonal and diurnal variations of raindrop size distribution in Asian monsoon region. *J. Meteor. Soc. Japan* **2006**, *84*, 195–209. [CrossRef]
30. Sun, Q.; Miao, C.; Duan, Q. Changes in the Spatial Heterogeneity and Annual Distribution of Observed Precipitation across China. *J. Clim.* **2017**, *30*, 9399–9416. [CrossRef]
31. Tokay, A.; Wolff, D.B.; Petersen, W.A. Evaluation of the New Version of the Laser-Optical Disdrometer, OTT Parsivel2. *J. Atmos. Oceanic Technol.* **2014**, *31*, 1276–1288. [CrossRef]
32. Löffler-Mang, M.; Joss, J. An optical distrometer for measuring size and velocity of hydrometeors. *J. Atmos. Ocean. Technol.* **2000**, *17*, 130–139. [CrossRef]

33. Atlas, D.; Srivastava, R.C.; Sekhon, R.S. Doppler radar characteristics of precipitation at vertical incidence. *Rev. Geophys.* **1973**, *11*, 1–35. [CrossRef]
34. Tokay, A.; Bashor, P.G. An experimental study of small-scale variability of raindrop size distribution. *J. Appl. Meteorol. Climatol.* **2010**, *49*, 2348–2365. [CrossRef]
35. Friedrich, K.; Kalina, E.A.; Masters, F.J. Drop-size distributions in thunderstorms measured by optical disdrometers during VORTEX2. *Mon. Weather Rev.* **2013**, *141*, 1182–1203. [CrossRef]
36. Wen, L.; Zhao, K.; Zhang, G.; Xue, M.; Zhou, B.; Liu, S.; Chen, X. Statistical characteristics of raindrop size distributions observed in East China during the Asian summer monsoon season using 2-D video disdrometer and Micro Rain Radar data. *J. Geophys. Res. Atmos.* **2016**, *121*, 2265–2282. [CrossRef]
37. Ulbrich, C.W. Natural variations in the analytical form of the drop size distribution. *J. Clim. Appl. Meteor.* **1983**, *22*, 1764–1775. [CrossRef]
38. Ulbrich, C.W.; Atlas, D. Rainfall microphysics and radar properties: Analysis methods for drop size spectra. *J. Appl. Meteorol.* **1998**, *37*, 912–923. [CrossRef]
39. Testud, J.; Oury, S.; Black, R.A.; Amayenc, P.; Dou, X. The Concept of "Normalized" Distribution to Describe Raindrop Spectra: A Tool for Cloud Physics and Cloud Remote Sensing. *J. Appl. Meteor.* **2001**, *40*, 1118–1140. [CrossRef]
40. Willis, P.T. Functional fits to some observed drop size distributions and parameterization of rain. *J. Atmos. Sci.* **1984**, *41*, 1648–1661. [CrossRef]
41. Sempere Torres, D.; Porrà, J.M.; Creutin, J.D. A general formulation for raindrop size distribution. *J. Appl. Meteor.* **1994**, *33*, 1494–1502. [CrossRef]
42. Sempere Torres, D.; Porrà, J.M.; Creutin, J.D. Experimental evidence of a general description for raindrop size distribution properties. *J. Geophys. Res.* **1998**, *103*, 1785–1797. [CrossRef]
43. Skofronick-Jackson, G.; Petersen, W.A.; Berg, W.; Kidd, C.; Stocker, E.F.; Kirschbaum, D.B.; Kakar, R.; Braun, S.A.; Huffman, G.J.; Iguchi, T.; et al. The Global Precipitation Measurement (GPM) mission for science and society. *Bull. Amer. Meteor. Soc.* **2017**, *98*, 1679–1695. [CrossRef]
44. Kotsuki, S.; Terasaki, K.; Miyoshi, T. GPM/DPR precipitation compared with a 3.5-km-resolution NICAM simulation. Scientific online letters on the atmosphere. *SOLA* **2014**, *10*, 204–209. [CrossRef]
45. Chandrasekar, V.; Le, M. Evaluation of profile classification module of GPM-DPR algorithm after launch. In Proceedings of the IEEE International Geoscience and Remote Sensing Symposium (IGARSS), Milan, Italy, 26–31 July 2015; pp. 5174–5177. [CrossRef]
46. Zhang, A.; Fu, Y. The structural characteristics of precipitation cases detected by dual-frequency radar of GPM satellite. *Chin. J. Atmos. Sci.* **2018**, *42*, 33–51. (In Chinese)
47. Iguchi, T.; Kozu, T.; Kwiatkowski, J.; Meneghini, R.; Awaka, J.; Okamoto, K. Uncertainties in the Rain Profiling Algorithm for the TRMM Precipitation Radar. *J. Meteor. Soc. Japan.* **2009**, *87*, 1–30. [CrossRef]
48. Bringi, V.N.; Chandrasekar, V.; Hubbert, J.; Gorgucci, E.; Randeu, W.L.; Schoenhuber, M. Raindrop size distribution in different climatic regimes from disdrometer and dual-polarized radar analysis. *J. Atmos. Sci.* **2003**, *60*, 354–365. [CrossRef]
49. Meagher, J.P.; Haddad, Z.S. To what extent can raindrop size be determined by a multiple-frequency radar? *J. Appl. Meteor. Climatol.* **2006**, *45*, 529–536. [CrossRef]
50. Zhang, G.; Vivekanandan, J.; Brandes, E.A.; Meneghini, R.; Kozu, T. The shape-slope relation in observed gamma raindrop size distributions: Statistical error or useful information? *J. Atmos. Ocean. Technol.* **2003**, *20*, 1106–1119. [CrossRef]
51. Chen, B.; Yang, J.; Pu, J. Statistical Characteristics of Raindrop Size Distribution in the Meiyu Season Observed in Eastern China. *J. Meteor. Soc. Japan* **2013**, *91*, 215–227. [CrossRef]
52. Cao, Q.; Zhang, G.; Brandes, E.; Schuur, T.; Ryzhkov, A.; Ikeda, K. Analysis of video disdrometer and polarimetric radar data to characterize rain microphysics in Oklahoma. *J. Appl. Meteorol. Climatol.* **2008**, *47*, 2238–2255. [CrossRef]
53. Vivekanandan, J.; Zhang, G.; Brandes, E. Polarimetric radar estimators based on a constrained gamma drop size distribution model. *J. Appl. Meteorol.* **2004**, *43*, 217–230. [CrossRef]

54. Atlas, D.; Ulbrich, C.W. Drop size spectra and integral remote sensing parameters in the transition from convective to stratiform rain. *Geophys. Res. Lett.* **2006**, *33*, L16803. [CrossRef]
55. Brandes, E.A.; Zhang, G.; Vivekanandan, J. An evaluation of a drop distribution–based polarimetric radar rainfall estimator. *J. Appl. Meteorol.* **2003**, *42*, 652–660. [CrossRef]